ORIGINAL PAPER

Thermal treatment of the tourmaline Fe-rich princivalleite Na(Mn$_2$Al)Al$_6$(Si$_6$O$_{18}$)(BO$_3$)$_3$(OH)$_3$O

Alessandra Altieri[1] · Riccardo Luppi[1] · Henrik Skogby[2] · Ulf Hålenius[2] · Gioacchino Tempesta[3] · Federico Pezzotta[4] · Ferdinando Bosi[1]

Abstract

Natural Fe^{2+}-rich princivalleite was thermally treated in the air at 700 °C to study crystal-chemical and color variations due to changes in oxidation states of Fe and Mn and atom ordering. Overall, the experimental data (electron microprobe, structural refinement, Mössbauer, infrared, and optical absorption spectroscopy) show that thermal treatment of princivalleite results in an almost total Fe^{2+} oxidation to Fe^{3+} and an oxidation of approximately one-third of Mn^{2+} to Mn^{3+} along with a minor degree of disorder of Al–Fe–Mn over the Y and Z sites. This process is accompanied by a significant deprotonation of the sample. The ^{Y}Fe and ^{Y}Mn oxidation from + 2 to + 3 yields in a decrease in a-parameter, whereas the increased content of ^{Z}Fe^{3+} results in a minor increase in the c-parameter. Optical absorption spectroscopy shows that the faint blue (azure) color of untreated princivalleite is caused by the presence of Fe^{2+} and the absence of Ti^{4+}. Thermal treatment in air (700 °C) changed the color to dark brown due to the progressive oxidation of Fe^{2+} to Fe^{3+} and Mn^{2+} to Mn^{3+}, as demonstrated by the evolution of optical absorption bands caused by electron transitions in these 3d-cations. However, the most evident result of the thermal treatment of the Fe-rich princivalleite sample is the simultaneous presence of Fe^{2+}, Fe^{3+}, Mn^{2+}, and Mn^{3+}, with a Fe^{3+}/ΣFe and Mn^{3+}/ΣMn ratio of 0.92 and 0.25, respectively. This observation suggests that the oxidation process during the heating experiments was largely controlled by kinetic factors.

Keywords Tourmaline · Thermally treated princivalleite · Chemical analyses · Spectroscopic analyses · Crystal structure analysis

Introduction

Minerals of the tourmaline supergroup are cyclosilicates with essential B. They are the most common and the earliest boron minerals formed on Earth and are widespread in the Earth's crust, occurring typically in granites and granitic pegmatites but also sedimentary and metamorphic rocks (Henry and Dutrow 1992, 1996; Grew et al. 2016). In accordance with Henry et al. (2011), the general formula of tourmaline, XY$_3$Z$_6$T$_6$O$_{18}$(BO$_3$)$_3$V$_3$W, represents many constituents: X = Na$^+$, K$^+$, Ca^{2+}, □ (= vacancy); Y = Al^{3+}, Fe^{3+}, Cr^{3+}, V^{3+}, Mg^{2+}, Fe^{2+}, Mn^{2+}, Li$^+$; Z = Al^{3+}, Fe^{3+}, Cr^{3+}, V^{3+}, Mg^{2+}, Fe^{2+}; T = Si^{4+}, Al^{3+}, B^{3+}; B = B^{3+}; V = (OH)$^-$, O^{2-}; W = (OH)$^-$, F$^-$, O^{2-}. Note that the not italicized letters X, Y, Z, and B represent groups of cations at the $^{[9]}X$, $^{[6]}Y$, $^{[6]}Z$, $^{[4]}T$, and $^{[3]}B$ crystallographic sites (letters italicized). The letters V and W represent groups of anions accommodated at the [3]-coordinated O3 and O1 crystallographic sites, respectively.

Minerals of the tourmaline supergroup are commonly used for understanding crustal evolution (e.g., Slack and Trumbull 2011). Because tourmaline has wide chemical and physical stability fields and its composition generally reflects the local environment of formation, it is of major petrogenetic interest (e.g., Dutrow and Henry 2011; Lussier et al.

✉ Alessandra Altieri
  alessandra.altieri@uniroma1.it

✉ Ferdinando Bosi
  ferdinando.bosi@uniroma1.it

1 Department of Earth Sciences, Sapienza University of Rome, P. Aldo Moro, 5, 00185 Rome, Italy

2 Department of Geosciences, Swedish Museum of Natural History, Box 50007, 10405 Stockholm, Sweden

3 Dipartimento di Scienze Della Terra e Geoambientali, Università degli Studi di Bari Aldo Moro, Bari, Italy

4 MUM–Mineralogical Museum "Luigi Celleri", via Cavour 73, San Piero in Campo, Campo nell'Elba, Leghorn, Italy

2008, 2011; Hinsberg and Schumacher 2011; van Hinsberg et al. 2011; Altieri et al. 2022, 2023). In this regard, it is of interest to perform high-temperature experiments on well-characterized tourmaline single crystals containing important elements, such as Mg, Al, Mn, and Fe, to reveal their thermally induced crystal-chemical behavior over the Y and Z sites, changes in the oxidation states, and color variations. Recently, Fe^{3+}-bearing schorl, oxy-dravite, Fe-free dravite, Fe-rich fluor-elbaite, fluor-tsilaisite, and Mn-bearing elbaite were thermally treated in air or hydrogen atmospheres (Afonina et al. 1993; Pieczka and Kraczka 2004; Bačĺk et al. 2011; Filip et al. 2012; Ertl et al. 2012; Bosi et al. 2016a, b, 2019; Liu et al. 2019). However, no similar study has addressed Fe-rich tourmalines with dominant Mn. The aim of this study is to understand the crystal-chemical and color variations in a princivalleite, ideally $Na(Mn_2Al)Al_6(Si_6O_{18})(BO_3)_3(OH)_3O$, as a function of temperature under oxidizing conditions. The Fe^{2+}-rich princivalleite crystal from princivalleite holotype material from Veddasca Valley, Luino area, Varese, Lombardy, Italy (Bosi et al. 2022) was used for the present study. Untreated and treated samples were structurally and chemically characterized by X-ray single-crystal diffraction, electron microprobe analysis, micro-laser induced breakdown spectroscopy, Mössbauer, infrared, and optical absorption spectroscopy.

Analytical methods

Thermal treatment

A crystal fragment of princivalleite was cut parallel to the **c**-axis and doubly polished to a thickness of 270 μm. Heat treatments were performed at 700 °C in air, with the sample placed in a gold container and inserted into a pre-heated horizontal tube furnace equipped with a quartz-glass tube. The experiments were performed stepwise, with heating times of 0.33, 1.7, 5, 21, and 86 h, and were ended by pushing the sample container out to the cold zone of the quartz tube, which caused the sample to cool to below 100 °C within 1 min. Spectroscopic data (FTIR and OAS) were acquired on the untreated sample and after each heating experiment. After the 21-h heating experiment, some of the bands in the OAS spectrum showed too high intensities, and the sample was further thinned to a thickness of 117 μm. Throughout this work, the untreated and heat-treated princivalleite samples are indicated as Upva and Tpva (respectively).

Microprobe analysis

Electron microprobe analysis was obtained using a wavelength dispersive spectrometer (WDS mode) with a Cameca SX50 instrument at the "Istituto di Geologia Ambientale e

Geoingegneria (Rome, Italy), CNR", operating at an accelerating potential of 15 kV, a sample current of 15 nA and 10 μm beam diameter. Minerals and synthetic compounds were used as standards: wollastonite (Si and Ca), magnetite (Fe), rutile (Ti), corundum (Al), vanadinite (V) fluorophlogopite (F), periclase (Mg), jadeite (Na), orthoclase (K), sphalerite (Zn), rhodonite (Mn), and metallic Cr and Cu. The PAP routine was applied (Pouchou and Pichoir 1991). The composition (mean of seven spot analyses) is given in Table 1. Titanium, V, Cr, and K were below detection limits (<0.03 wt.%).

Micro-laser-induced breakdown spectroscopy

The micro-Laser-Induced Breakdown Spectroscopy (μ-LIBS) instrument used for Li measurement integrates a dual-pulse Q-Switched laser (Nd-YAG, fundamental $\lambda = 1064$ nm), which emits two collinear laser pulses with energy of 110 mJ per pulse at 10 Hz, and the reciprocal delay was set at 1 μs.

The coupling of the laser with a petrographic microscope with a 10× objective lens (NA = 0.25 and WD = 14.75 mm) allows to obtain a very small spot size (7–10 μm). The

Table 1 Chemical data (seven spots) for the princivalleite untreated (Upva) and treated (Tpva)

wt%	Upva	Tpva
SiO_2	34.41 (46)	–
B_2O_3[a]	10.62	–
Al_2O_3	41.46 (27)	–
FeO_{EMPA}	3.79 (12)	–
MnO_{EMPA}	5.28 (14)	–
MgO	0.08 (3)	–
ZnO	0.22 (7)	–
CaO	0.72 (6)	–
Na_2O	1.71 (5)	–
Li_2O[b]	0.11 (4)	–
F	0.40 (11)	–
H_2O[a]	2.57	1.96
O=F	−0.17	–
FeO[c]	3.79	0.30
Fe_2O_3[c]	0	3.87
MnO[d]	5.28	3.94
Mn_2O_3[d]	0	1.49
Total	101.19	100.75

Chemical data for Tpva are the same as Upva, except for FeO, Fe_2O_3, MnO, and Mn_2O_3 (see text)

[a]Calculated by stoichiometry, $(Y+Z+T) = 15.00$ and 31 anions

[b]Determined by μ-laser induced breakdown spectroscopy

[c]Determined by Mössbauer spectroscopy

[d]Determined by optical absorption spectroscopy

μ-LIBS spectra were acquired using an AvaSpec Fiber Optic Spectrometer (390–900 nm with 0.3 nm resolution) with a delay of 2 μs after the second pulse and were integrated for 1 ms. Quantitative data were obtained by generating a linear regression using the main Li emission line intensity (670.706 nm corresponding to resonance transition $1s^2 2s > 1s^2 2p$) particularly sensitive to Li amounts. The linear fit was made according to Bosi et al. (2021) and revealed amounts of $Li_2O = 0.11(4)$ wt.% (Table 1) in line with that estimated by Pesquera et al.'s (2016) method (0.08 Li_2O wt.%).

Single-crystal structure refinement

Crystal fragments of samples Upva and Tpva (700 °C) were selected for X-ray diffraction measurements on a Bruker KAPPA APEX-II single-crystal diffractometer (at Sapienza University of Rome, Earth Sciences Department), equipped with a CCD area detector (6.2×6.2 cm^2 active detection area, 512×512 pixels) and a graphite-crystal monochromator, using Mo$K\alpha$ radiation from a fine-focus sealed X-ray tube. The sample-to-detector distance was 4 cm. A total of 1621 exposures were measured (step = 0.4°, time/step = 20 s) covering the full reciprocal sphere with a redundancy up to 12 and a completeness of about 98%. Final unit-cell parameters were refined with the Bruker AXS SAINT program using reflections with $I > 10 \sigma_I$ in the range $5° < 2\theta < 75°$. The intensity data were processed and corrected for Lorentz, polarization, and background effects with the APEX2 software program of Bruker AXS. The data were corrected for absorption using the multi-scan method (SADABS), leading to a significant improvement in R_{int}. No violations of $R3m$ symmetry were noted.

Structure refinement was done with the SHELXL-2013 program (Sheldrick 2013). Starting coordinates were taken from Bosi et al. (2022). Variable parameters were: scale factor, extinction coefficient, atom coordinates, site-scattering values, and atom-displacement factors. In detail, the X site was modeled by considering the presence of the Na scattering factor; the Y site was modeled considering Al–Mn for Upva and Al–Fe for Tpva; the occupancy of the Z site was modeled considering Al and Fe. The T, B, and anion sites were modeled, respectively, with Si, B, and O scattering factors and with a fixed occupancy of 1, because refinement with unconstrained occupancies showed no significant deviations from this value. The position of the H atom bonded to the oxygen at the O3 site in the structure was taken from the difference-Fourier map and incorporated into the refinement model; the O3–H3-bond length was restrained (by DFIX command) to be 0.97 Å with the isotropic-displacement parameter constrained to be equal to 1.2 times that obtained for the O3 site. Three full-matrix refinement cycles with isotropic-displacement parameters for all atoms were followed by anisotropic cycles until convergence was attained. There were no significant correlations over 0.7 between the parameters at the end of refinement. Table 2 lists crystal data, data-collection information, and refinement details; Table 3 gives the fractional atom coordinates and site occupancies; Table 4 gives selected bond distances. The crystallographic information file has been deposited with the Principal Editor of Physics and Chemistry of Minerals and is available as Supplementary material (see below).

Mössbauer spectroscopy

After the final thermal treatment, sample Tpva was analyzed by Mössbauer spectroscopy (MS) using a conventional spectrometer system equipped with a 10 mCi point source and operated in constant acceleration mode. The absorber was prepared by grinding small amounts of sample material together with a thermoplastic resin, which were then shaped into a 1-mm sized cylinder under mild heating (ca. 100 °C). The spectrum was collected at room temperature over the velocity range – 4.2 to + 4.2 mm^{-1} and was calibrated against α-Fe foil before folding and spectral fitting with the software MossA (Prescher et al. 2012).

Infrared spectroscopy

Fourier-transform infrared (FTIR) spectroscopy was used to characterize the (OH) vibrational absorption bands of the sample before and after each thermal treatment. The spectrometer system consisted of a Bruker Vertex 70 spectrometer equipped with a halogen-lamp source and a CaF$_2$ beamsplitter coupled to a Hyperion 2000 microscope with a ZnSe wire-grid polarizer and an InSb detector. Polarized spectra were collected parallel and perpendicular to the **c**-axis over the wavenumber range 2000–12000 cm^{-1} with a resolution of 4 cm^{-1}. The measuring areas were masked by a ~ 100 μm rectangular aperture to avoid cracks and inclusions.

Optical absorption spectroscopy

Polarized optical absorption spectra were measured at room temperature on the same doubly polished single-crystal sections used for the FTIR measurements. Spectra in the range 270–1000 nm (37,037–10,000 cm^{-1}) were recorded at a spectral resolution of 1 nm using an AVASPEC-ULS2048X16 spectrometer (at the Swedish Museum of Natural History) connected with a 400 μm UV fiber cable to a Zeiss Axiotron UV-microscope. A 75 W Xenon arc lamp was used as a light source, and Zeiss Ultrafluar 10× lenses served as objective and condenser. The diameter of the circular aperture was 40 μm. A UV-quality Glan–Thompson prism with a working range from 250 to 2700 nm (40,000 to 3704 cm^{-1}) was used as a polarizer. The wavelength scale of the spectrometers

Table 2 Single-crystal X-ray diffraction data details for princivalleite untreated (Upva) and treated (Tpva)

	Upva	Tpva
Crystal size (mm)	$0.22 \times 0.20 \times 0.20$	$0.20 \times 0.20 \times 0.06$
a (Å)	15.91620 (19)	15.8323 (2)
c	7.11485 (9)	7.1312 (1)
V (Å^3)	1560.90 (4)	1548.04 (4)
Axis, frame width (°), time per frame (s)	Phi-omega, 0.4, 20	Phi-omega, 0.4, 20
Reciprocal space range hkl	$-26 \leq h \leq 21$; $-25 \leq k \leq 24$; $-11 \leq l \leq 12$	$-22 \leq h \leq 23$; $-26 \leq k \leq 26$; $-10 \leq l \leq 11$
Set of read reflections	11,555	10,897
Unique reflections, R_{int} (%)	1900, 1.70	1811, 2.09
Unique reflections with $I > 2\sigma_I$	1884	1748
Redundancy	12	11
Restraints, refined parameters	1, 94	1, 93
Extinction coefficient	0.00029 (14)	–
Flack parameter	−0.04 (2)	−0.03 (3)
wR2 all data (%)	3.14	3.82
R1 (%) all data	1.30	1.86
R1 (%) for $I > 2\sigma_I$	1.26	1.69
GooF	1.081	1.084
Largest diff. peak and hole (e^-/Å^3)	−0.25 and 0.69	−0.42 and 0.31

Radiation, Mo$K\alpha = 0.71073$ Å. Data-collection temperature = 293 K. Range for data collection, $5° < 2\theta < 76°$. Absorption correction method: multi-scan (SADABS). Refinement method: Full-matrix least-squares on F^2. Structural refinement program: SHELXL-2013. Space-group type $R3m$; $Z = 3$

R_{int} merging residual value, $R1$ discrepancy index, calculated from F-data, $wR2$ weighted discrepancy index, calculated from F^2-data, $GooF$ goodness of fit, *Diff. Peaks* maximum and minimum residual electron density

was calibrated against Ho_2O_3-doped and Pr_2O_3/Nd_2O_3-doped standards (Hellma glass filters 666F1 and 666F7). Spectral data in the range 10,000–5000 cm^{-1} (1000–2000 nm) were taken from the FTIR measurements. Recorded spectra were fitted using the Jandel PeakFit 4.12 software, assuming Gaussian peak shapes.

Results and discussion

The color of the untreated crystal is very pale blue (azure). During the steps of heat treatment, it darkens, and the color changes via shades of gray to very dark brown (Fig. 1).

Mössbauer spectra: oxidation state of Fe

The spectrum of the heat-treated sample (Tpva) was fitted using Lorentzian doublets. In agreement with Andreozzi et al. (2008), a model with three doublets was adopted (Fig. 2). The spectrum was fitted with two doublets assigned to Fe^{3+} and one doublet assigned to Fe^{2+}, confirming the presence of both Fe^{2+} and Fe^{3+} in the sample Tpva. The relatively broad absorption related to Fe^{3+} indicates that Fe^{3+} occurs at both the Y and Z sites. However, a unique site

distribution cannot be achieved due to lack of resolution. The resulting hyperfine parameters and absorption intensity areas are shown in Table 5. The spectrum of the heat-treated sample, compared to the spectrum of the untreated sample (see Fig. 2 in Bosi et al. 2022), shows a strongly increased absorption in the velocity range, typical for Fe^{3+}. The results from the fitting procedure indicate the Fe^{3+}/ΣFe ratio of 92% for the treated sample, whereas no indication of absorption due to Fe^{3+} was observed for untreated princivalleite (Bosi et al. 2022).

Optical spectra: oxidation state of Mn

The recorded spectra show two broad absorption bands at 13,500 and 8900 cm^{-1}. In the spectra of the untreated sample, these bands are moderately polarized in $\mathbf{E}\perp\mathbf{c}$ (Bosi et al. 2022). In addition to these two strong bands, there are weak and relatively narrow bands at ~18,000, ~22,500, ~24,000, and ~27,500 cm^{-1}, which are assigned to spin-forbidden electronic transitions in [6]-coordinated Mn^{2+} (Bosi et al. 2022).

During continued heat treatment up to 5 h, the 13,500 and 8900 cm^{-1} bands in spectra become progressively more intense and stronger polarized ($\mathbf{E}\perp\mathbf{c} > > \mathbf{E}\parallel\mathbf{c}$). However,

Table 3 Fractional atom coordinates, isotropic (*) or equivalent-isotropic-displacement parameters (in Å^2), and site occupancies (s.o.) for untreated (Upva) and treated (Tpva) princivalleite

	x	y	z	$U_{eq/iso}$	s.o
Upva					
X	0	0	0.2179 (3)	0.0177 (5)	Na$_{0.779(7)}$
Y	0.12295 (3)	0.06148 (2)	0.62973 (7)	0.00924 (11)	Al$_{0.662(4)}$Mn$_{0.338(4)}$
Z	0.29755 (2)	0.26105 (2)	0.60836 (6)	0.00526 (9)	Al$_{0.984(2)}$Fe$_{0.016(2)}$
B	0.10966 (6)	0.21932 (12)	0.4516 (2)	0.0059 (2)	B$_{1.00}$
T	0.19198 (2)	0.18997 (2)	0	0.00453 (6)	Si$_{1.00}$
O1 ≡ W	0	0	0.7731 (3)	0.0272 (6)	O$_{1.00}$
O2	0.06097 (5)	0.12194 (9)	0.48466 (18)	0.0156 (3)	O$_{1.00}$
O3 ≡ V	0.26467 (10)	0.13233 (5)	0.50703 (16)	0.0113 (2)	O$_{1.00}$
H3	0.2533 (19)	0.1266 (9)	0.380 (3)	0.014^a	H$_{1.00}$
O4	0.09388 (5)	0.18775 (9)	0.07144 (16)	0.0095 (2)	O$_{1.00}$
O5	0.18711 (9)	0.09355 (5)	0.09399 (16)	0.0100 (2)	O$_{1.00}$
O6	0.19625 (6)	0.18558(6)	0.77310 (12)	0.00695 (13)	O$_{1.00}$
O7	0.28651 (6)	0.28652 (5)	0.07740 (10)	0.00585 (13)	O$_{1.00}$
O8	0.20947 (6)	0.27033 (6)	0.43781 (12)	0.00676 (13)	O$_{1.00}$
Tpva					
X	0	0	0.2172 (4)	0.0191 (8)	Na$_{0.697(9)}$
Y	0.12375 (4)	0.06187 (2)	0.63139 (9)	0.00792 (13)	Al$_{0.697(4)}$Fe$_{0.303(4)}$
Z	0.29668 (3)	0.25904 (3)	0.60413 (9)	0.00657 (11)	Al$_{0.946(3)}$Fe$_{0.054(3)}$
B	0.10982 (8)	0.21963 (17)	0.4500 (3)	0.0062 (3)	B$_{1.00}$
T	0.19149 (3)	0.18999 (3)	0	0.00493 (8)	Si$_{1.00}$
O1 ≡ W	0	0	0.7598 (4)	0.0110 (5)	O$_{1.00}$
O2	0.06074 (6)	0.12147 (11)	0.4863 (2)	0.0093 (3)	O$_{1.00}$
O3 ≡ V	0.25840 (12)	0.12920 (6)	0.5116 (2)	0.0097 (3)	O$_{1.00}$
H3	0.245 (2)	0.1224 (11)	0.380 (3)	0.012^a	H$_{1.00}$
O4	0.09496 (6)	0.18992 (12)	0.0760 (2)	0.0094 (3)	O$_{1.00}$
O5	0.18518 (13)	0.09259 (6)	0.0911 (2)	0.0105 (3)	O$_{1.00}$
O6	0.19261 (7)	0.18416 (8)	0.77299 (16)	0.00712 (17)	O$_{1.00}$
O7	0.28706 (7)	0.28635 (7)	0.07445 (15)	0.00615 (17)	O$_{1.00}$
O8	0.20968 (7)	0.27069 (8)	0.43566 (16)	0.00659 (18)	O$_{1.00}$

^{a}Isotropic displacement parameters (U_{iso}) for H3 constrained to have a U_{iso} 1.2 times the U_{eq} value of the O3 oxygen atom

at 21 h of heat treatment, a decrease in their intensities is observed (Fig. 3). The lower intensity and the moderate polarization of these two absorption bands in spectra of the untreated princivalleite crystal are explained by its very low or non-existing Fe^{3+} concentration, and consequently, these two bands mark pure, or nearly so, Fe^{2+} d–d transitions in spectra of the untreated sample. Intensity increases, and a higher degree of $\mathbf{E}\perp\mathbf{c}$-polarization of the two bands during continued heat treatment of the sample is explained by progressive oxidation of Fe^{2+} to Fe^{3+} and consequently increasing Fe^{3+}-enhancement of band intensities in $\mathbf{E}\perp\mathbf{c}$. In agreement with previous optical studies of tourmaline (e.g., Mattson and Rossman 1984, 1987), the absorption bands at 13,500 and 8900 cm^{-1} in the heat-treated sample are assigned to Fe^{3+}-enhanced spin-allowed d–d transitions in six-coordinated Fe^{2+}. The intensity loss for the 13,500 and 8900 cm^{-1} bands recorded after 5 h of heat treatment

is explained by continued oxidation of Fe^{2+}, which results in a decrease in $[Fe^{2+}][Fe^{3+}]$ concentration product when $[Fe^{3+}] > > [Fe^{2+}]$.

After 5 h of heat treatment, an additional broad absorption band is observed at 17,900 cm^{-1}, and this band gain in intensity after continued heat treatment. In accordance with band assignments of spectra recorded on Mn-rich tourmaline samples (Reinitz and Rossman 1988; Taran et al. 1993; Ertl et al. 2005; Novák et al. 2013; Bosi et al. 2021), this band is ascribed to a Mn^{3+} spin-allowed transition.

The observed intensity increases of the UV-edge absorption marking O–M^{3+} charge transfer processes, in combination with a strong initial increase in intensity of the 13,500 and 8900 cm^{-1} bands in $\mathbf{E}\perp\mathbf{c}$-spectra followed by a subsequent decrease in their intensities during further heat treatment reflects a progressive Fe^{2+} to Fe^{3+} oxidation of the sample. The occurrence of a Mn^{3+} absorption band after

Table 4 Selected bond lengths (Å) for untreated (Upva) and treated (Tpva) princivalleite

	Upva	Tpva
X-O2 ($\times$3)	2.5354 (18)	2.541 (3)
X-O5 ($\times$3)	2.7255 (14)	2.6936 (19)
X-O4 ($\times$3)	2.7898 (14)	2.7919 (19)
$<X$-O$>$	2.684	2.676
Y-O1	1.9780 (13)	1.9280 (14)
Y-O2 ($\times$2)	1.9784 (8)	1.9742 (10)
Y-O6 ($\times$2)	1.9997 (9)	1.9611 (11)
Y-O3	2.1396 (14)	2.0344 (17)
$<Y$–O$>$	2.012	1.972
Z-O6	1.8654 (8)	1.9018 (11)
Z-O7	1.8751 (8)	1.8845 (11)
Z-O8	1.8869 (8)	1.8887 (11)
Z-O8'	1.9149 (8)	1.9049 (11)
Z-O7'	1.9416 (8)	1.9584 (11)
Z-O3	1.9796 (6)	1.9449 (8)
$<Z$-O$>$	1.911	1.914
B-O2	1.363 (2)	1.9018 (11)
B-O8 ($\times$2)	1.3794 (12)	1.8845 (11)
$<B$-O$>$	1.374	1.372
T-O7	1.6176 (8)	1.6094 (10)
T-O6	1.6188 (8)	1.6221 (12)
T-O4	1.6256 (5)	1.6211 (7)
T-O5	1.6398 (5)	1.6296 (7)
$<T$-O$>$	1.625	1.621

several hours of heat treatment demonstrates that oxidation of Mn^{2+} starts subsequent to the initial oxidation of Fe^{2+} to Fe^{3+}. The Mn_2O_3 content in the princivalleite sample subject to different heating times was calculated from the intensity of the Mn^{3+} band at 17,900 cm^{-1} in tourmaline spectra using the molar absorption coefficient (e) proposed by Bosi et al. (2021). Values of 0.27, 0.73, and 1.49 wt% were estimated in the sample subjected to 1.7, 5, and 21 h of heat treatment, respectively (Table 6).

Due to an extremely strong UV-edge absorption in the spectrum of the sample after 86 h treatment, it was not possible to record the Mn^{3+} band at 17,900 cm^{-1}, but its Mn_2O_3 content is expected to be > 1.5 wt%. It is interesting to point out that the oxidation of MnO follows a hyperbolic behavior, with an estimated maximum of Mn_2O_3 content of ~2.3 wt%, corresponding to a $Mn^{3+}/\Sigma Mn$ ratio of ~0.4.

Site populations

In agreement with the structure-refinement results, the boron content was assumed to be stoichiometric (B^{3+} = 3.00 apfu). Both the site-scattering results and the bond lengths of B and T are consistent with the B site being fully occupied by boron and no amount of B^{3+} at the T site (e.g., Bosi and Lucchesi 2007). Lithium was determined by µ-LIBS for sample Upva. The iron oxidation state was determined by Mössbauer spectroscopy. In accordance with the optical absorption spectroscopy results mentioned above, Mn is considered as Mn^{2+} for sample Upva, whereas it cannot be considered only Mn^{2+} for sample Tpva. Consequently, the Mn_2O_3 contents were fixed to 1.49 wt% for the treated sample based on bond-valence analysis and the direct correlation between bond-valence sum (BVS) at the O3 site, BVS(O3), and ^{O3}O contents (Bosi et al. 2018). The latter, in fact, suggests that Mn_2O_3 amount >> 1.5 wt% would produce Mn^{3+} apfu values that deviate too much from the expected trend (see Fig. 4). The (OH) content and the atoms per formula unit (apfu) were then calculated by charge balance with the assumption (T + Y + Z) = 15 apfu and 31 anions. Note that we assume that no compositional change occurred in the treated sample with respect to the untreated princivalleite, except for the contents of FeO, Fe_2O_3, MnO, and Mn_2O_3, which changed in accord with the $Fe^{3+}/\Sigma Fe$ and $Mn^{3+}/\Sigma Mn$ ratios (see above) and for the contents of O^{2-} and $(OH)^-$ needed to maintain charge balance. The very good agreement between the number of electrons per formula unit (epfu) derived from chemical data and X-ray single-crystal structure refinement (SREF), respectively, 224.4 and 224.7

Fig. 1 Images of the same Fe-rich princivalleite crystal untreated (Upva) and heat-heated (700 °C) for different times (1.7 h, 5 h and 21 h) showing color variation from faint blue (azure) to gray to dark brown. The polished plate is approximately 1 mm in length and 270 µm thick
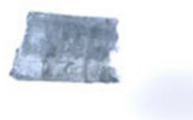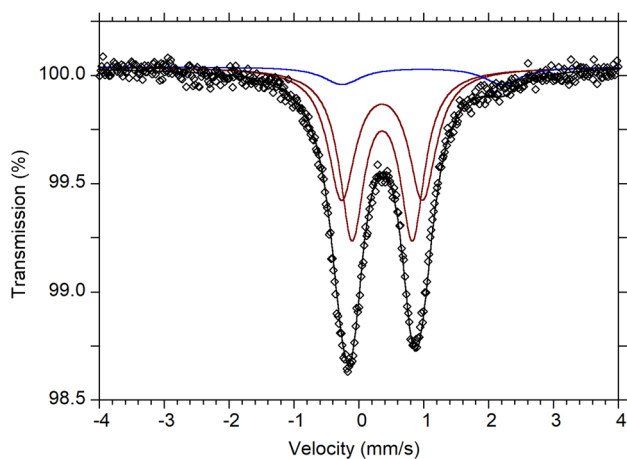
Fig. 2 Mössbauer spectrum obtained at room temperature for the fully heat-treated princivalleite sample (Tpva). Fitted absorption doublets assigned to Fe^{2+} and Fe^{3+} are indicated in blue and red, respectively. Diamonds denotes measured spectra, and black curve represents summed fitted spectra

epfu for Upva, and 223.0 and 224.3 epfu for Tpva, supports the stoichiometric assumptions.

The site populations were optimized on the procedure described in Bosi et al. (2017). The robustness of this optimized cation distribution was successively confirmed by the procedure of Wright et al. (2000). The final structural formulae for the studied samples are as follows.

Table 5 Mössbauer parameters for treated princivalleite sample (Tpva) obtained at room temperature

δ (mm/s)	ΔE_Q (mm/s)	FWHM (mm/s)	Area (%)	Assignment
0.36	1.25	0.51	43.1	$^{VI}Fe^{3+}$
0.35	0.93	0.46	49.1	$^{VI}Fe^{3+}$
0.98	2.47	0.69	7.8	$^{VI}Fe^{2+}$

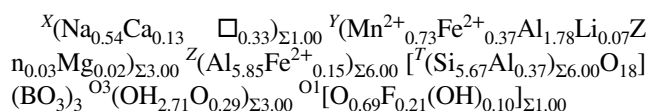δ centroid shift, ΔE_Q quadrupole splitting, *FWHM* full width at half-maximum
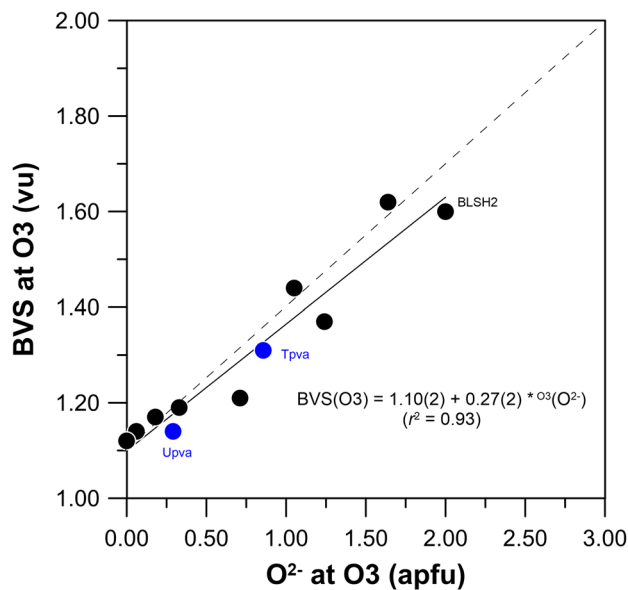
Fig. 4 Plot of bond-valence sum (BVS) incidents at the O3 site versus oxygen content at the O3 site (after Bosi et al. 2018). Solid line is the linear regression showing the empirical trend, whereas dashed line is the expected trend. Plot obtained using 11 data sets accompanied by SREF. Black circles = samples from Bosi et al. (2018), including sample BLSH2 (Ertl et al. 2012). Blue circles = samples from this study

Fig. 3 Optical absorption spectra polarized in **E**⊥**c** of untreated and stepwise heat-treated (700 °C) princivalleite. The main absorption bands are indicated

Table 6 Oxidation of MnO in the princivalleite sample at different heating times

Heating time (hrs)	Net linear absorption coefficient (cm^{-1})	Mn_2O_3-concentration (wt%)
1.7	3.2	0.27
5.0	8.8	0.73
21.0	17.9	1.49

The concentration in Mn_2O_3 is calculated from net linear absorption values considering the intensity of the Mn^{3+}-band at 17,900 cm^{-1} in combination with the molar extinction coefficient of ~30 l $mole^{-1}$ cm^{-1} (as proposed in Bosi et al. 2021)

Sample Upva

$^X(Na_{0.54}Ca_{0.13} \square_{0.33})_{\Sigma 1.00} {}^Y(Mn^{2+}_{0.73}Fe^{2+}_{0.37}Al_{1.78}Li_{0.07}Zn_{0.03}Mg_{0.02})_{\Sigma 3.00} {}^Z(Al_{5.85}Fe^{2+}_{0.15})_{\Sigma 6.00} [{}^T(Si_{5.67}Al_{0.37})_{\Sigma 6.00}O_{18}] (BO_3)_3 {}^{O3}(OH_{2.71}O_{0.29})_{\Sigma 3.00} {}^{O1}[O_{0.69}F_{0.21}(OH)_{0.10}]_{\Sigma 1.00}$

Sample Tpva (700 °C)

$^X(Na_{0.54}Ca_{0.13} \square_{0.33})_{\Sigma 1.00} {}^Y(Mn^{2+}_{0.40}Fe^{2+}_{0.04}Fe^{3+}_{0.33}Mn^{3+}_{0.19}Al_{1.93}Li_{0.07}Zn_{0.03}Mg_{0.02})_{\Sigma 3.00} {}^Z(Al_{5.70}Fe^{3+}_{0.15} Mn^{2+}_{0.15})_{\Sigma 6.00} [{}^T(Si_{5.63}Al_{0.37})_{\Sigma 6.00}O_{18}] (BO_3)_3 {}^{O3}[(OH)_{2.14}O_{0.86}]_{\Sigma 3.00} {}^{O1}(O_{0.79}F_{0.21})_{\Sigma 1.00.}$
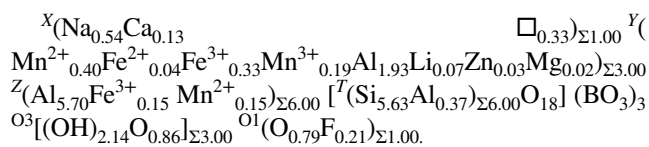
A comparison between the values of refined site-scatterings and mean bond lengths and those calculated from this site population is reported in Table 7. The agreement between the refined and calculated values is very good, and validates the distribution of cations over the Y and Z sites in the empirical structural formula of samples Upva and Tpva. This site population is also supported by the comparison of weighted BVS and mean formal charge (weighted atomic valence) calculated from the empirical structural formula (Table 8).

FTIR spectra in the (OH)-stretching region and band assignment

The infrared spectra of the untreated sample (Upva) recorded in the polarized mode both perpendicular and parallel to the **c** direction show (OH) band positions very similar to those observed in the holotype material described by Bosi et al. (2022). In detail, spectra recorded in polarized mode parallel to the crystallographic **c**-axis (**E∥c**) show a significant band at 3365 cm^{-1}, a very intense band around 3500 cm^{-1}, two weaker bands at 3632 and 3644 cm^{-1}, and two very weak bands at 3662 and 3671 cm^{-1} (Fig. 3 of Bosi et al. 2022). As observed typically for tourmaline spectra in the (OH) range, the main band is off-scale for the **E∥c** direction due to excessive absorption, whereas spectra obtained perpendicular to

the **c**-axis (**E⊥c**) show considerably weaker bands (Fig. 3 of Bosi et al. 2022). In accordance with Watenphul et al. (2016), Bosi et al. (2022) assigned these bands as follows: the band at 3365 cm^{-1} is consistent with the presence of minor Al along with Si in [4]-fold coordination, and the main band FTIR bands at ~3500 cm^{-1} are likely caused by the occurrence of the atomic arrangements $3[{}^Y(Fe, Mn, Al)^ZAl^ZAl]–^{O3}(OH)_3$, whereas the bands above 3600 cm^{-1} may be caused by the arrangements $^Y[(Li, Fe, Mn)(Fe, Mn, Al)Al]–^{O1}(OH)–^X(\square)$. However, alternative assignments of atomic arrangements are possible by considering the model proposed by Fuchs et al. (2022) and Balan et al. (2023). The **E∥c**-spectrum of the Upva sample reported in Fig. 5a shows only the two weak bands at 3662 and 3671 cm^{-1}, while the other bands are off-scale.

Spectra acquired after the stepwise heating experiments at 700 °C show significant changes (Fig. 5a). For spectra polarized parallel to the **c**-axis (**E∥c**), the relatively large thickness of the sample obscures the strong fundamental (OH) bands. However, the weaker bands that occur at 3644, 3662, and 3671 cm^{-1} show a continuous decrease in intensity after each heating step and are chiefly absent after the last treatment. The (OH) overtone bands in the range 6700–7200 cm^{-1} also indicate substantial dehydrogenation during the heat treatments (Fig. 5b). It is apparent that the bands at higher wavenumbers, related to $^{O1}(OH)$, decrease faster than bands occurring at lower wavenumbers related to $^{O3}(OH)$.

Based on the result from Mössbauer spectroscopy as well as optical absorption spectroscopy with the Fe^{3+}-enhanced Fe^{2+} band about 9000 cm^{-1} (Fig. 3) showing an increase in intensity after the sequential heating experiments, the following redox reaction occurred:
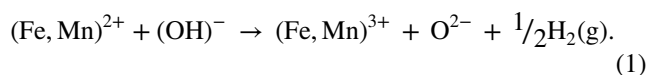
$$(Fe, Mn)^{2+} + (OH)^- \rightarrow (Fe, Mn)^{3+} + O^{2-} + \tfrac{1}{2}H_2(g). \tag{1}$$

Table 7 Optimized Y and Z site-populations (apfu[b]), site-scattering (epfu[a]), and mean bond-length (Å) values for untreated (Upva) and treated (Tpva) princivalleite

Site	Optimized site population	Site-scattering		Mean bond length	
		Obs	Calc	Obs	Calc.[c]
	Upva				
Y	$Mn^{2+}_{0.73}Fe^{2+}_{0.37}Al_{1.78}Li_{0.07}Zn_{0.03}Mg_{0.02}$	51.2 (2)	52.3	2.012	2.009
Z	$Al_{5.85}Fe^{2+}_{0.15}$	79.3 (2)	79.9	1.911	1.909
	Tpva				
Y	$Mn^{2+}_{0.40}Fe^{2+}_{0.04}Fe^{3+}_{0.33}Mn^{3+}_{0.19}Al_{1.93}Li_{0.07}Zn_{0.03}Mg_{0.02}$	50.8 (2)	50.5	1.972	1.974
Z	$Al_{5.70}Fe^{3+}_{0.15} Mn^{2+}_{0.15}$	82.2 (3)	81.7	1.914	1.914

[a]Electrons per formula unit

[b]Atoms per formula unit

[c]Ionic radii from Bosi (2018)

Table 8 Weighted bond valences (valence units) for untreated (Upva) and treated (Tpva) princivalleite

	X	Y	Z	T	B	Σ_{anion}
Upva						
O1		3×→0.45				1.35
O2	0.10↓×3	2×→0.47↓×2			1.02	2.06
O3		0.30	2×→0.42			1.14
O4	0.05↓×3			2×→0.99		2.03
O5	0.06↓×3			2×→0.99		1.98
O6		0.44↓×2	0.56	1.01		2.02
O7			0.55	1.02		2.02
			0.46			
O8			0.49		0.98↓×2	2.00
			0.53			
Σ_{cation}	0.64	2.57	3.01	3.98	2.98	
MFC[a]	0.79	2.57	2.98	3.94	3.00	
Tpva						
O1		3×→0.50				1.51
O2	0.10↓×3	2×→0.46↓×2			1.00	2.02
O3		0.39	2×→0.46			1.31
O4	0.05↓×3			2×→1.01		2.07
O5	0.07↓×3			2×→0.98		2.04
O6		0.48↓×2	0.52	1.01		2.00
O7			0.54	1.04		2.02
			0.44			
O8			0.51		0.99↓×2	2.04
			0.54			
Σ_{cation}	0.65	2.77	3.02	4.04	2.99	
MFC[a]	0.79	2.79	2.98	3.94	3.00	

Weighted bond valence according to Bosi (2014). Bond valence parameters for cation-O bonds from Brown and Altermatt (1985)

[a]Mean formal charge (or weighted atomic valence) from the empirical structural formula
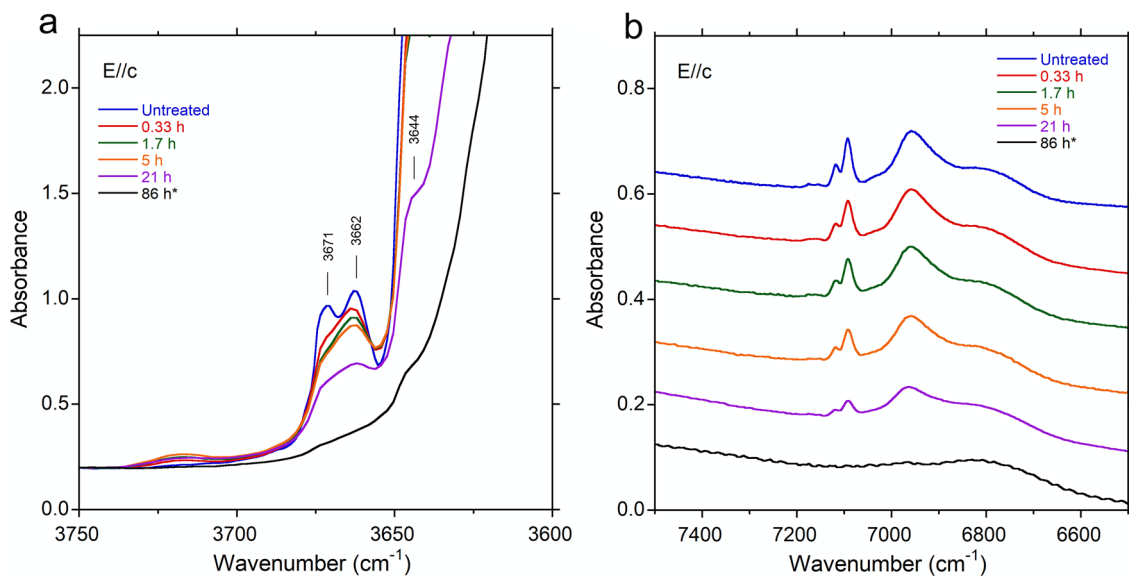
Fig. 5 Polarized FTIR spectra (**E**‖**c**) of untreated and stepwise heat-treated (700 °C) princivalleite: **a** fundamental (OH) region and **b** (OH) overtone region. Spectra have been vertically adjusted for clarity. Peak positions are indicated. Sample thickness 270 μm. * = sample thinned to 117 μm, but spectrum normalized to the original thickness of 270 μm

It is worth noting that the weak bands above ~ 3600 cm^{-1} observed for the untreated sample are consistent with low concentrations of ^{O1}(OH) obtained from the other methods. Similarly, the lack of bands above ~ 3600 cm^{-1} after the final treatment is consistent with the absence of ^{O1}(OH). Moreover, with respect to the untreated sample, the strongly decreased band intensities in the (OH) overtone region (6700–7200 cm^{-1}) in the spectra of the treated sample are consistent with substantial deprotonation of the O3 site accompanied by oxidation of Fe and Mn from + 2 to + 3.

Crystal chemistry

Compositional differences between the untreated and treated samples occur in the $Fe^{3+}/\Sigma Fe$ and $Mn^{3+}/\Sigma Mn$ ratios (zero for untreated and, respectively, 0.92 and 0.25 for Tpva heated at 700 °C), and in (OH) contents (2.71 apfu for untreated, 2.14 apfu for Tpva) as a result of the redox reaction (1).

The structural data show that the treated Tpva sample is somewhat different from the untreated Upva: for instance, the unit-cell parameter a decreased from 15.9162(2) Å in Upva to 15.8323(2) Å in Tpva, whereas the c-parameter increased from 7.11485(9) Å in Upva to 7.13120(10) Å in Tpva (Table 2). Such a difference is also found by the variation in the refined site-scattering and mean bond-length values for the untreated–treated samples: e.g., the site-scattering of Y 51.2(2)–50.8(2) epfu and of Z 79.3(2)–82.2(3) epfu, < Y–O > 2.012–1.972 and < Z–O > Å 1.911–1.914 Å. All these variations reflect the almost total Fe oxidation from Fe^{2+} to Fe^{3+} and the oxidation of one-third amount of Mn from Mn^{2+} to Mn^{3+} along with a minor degree of disorder of Al–Fe–Mn over the Y and Z sites. On this basis, the observed decrease in the a-parameter is interpreted as a result of the Fe and Mn oxidation from + 2 to + 3, which occurred during the heating experiments, whereas the increase in the c-parameter is interpreted as a result of the Al–Fe–Mn disorder. This interpretation is consistent with other thermally treated tourmalines (Pieczka and Kraczka 2004; Bačík et al. 2011; Bosi et al. 2016a, 2018, 2019; Liu et al. 2019; Celata et al. 2021; Ballirano et al. 2022a, b, 2023; Hovis et al. 2023).

The most evident result of the thermal treatment of the Fe-rich princivalleite sample in the air at 700 °C is the simultaneous presence of Fe^{2+}, Fe^{3+}, Mn^{2+}, and Mn^{3+}, which suggests that the oxidation process during the heating experiments was largely controlled by kinetic factors, with an almost total oxidation of Fe^{2+} to Fe^{3+} and a fair degree of oxidation of Mn^{2+} to Mn^{3+}. This process is accompanied by significant deprotonation of the (OH) groups at the O1 and O3 sites (the $^V O^{2-}$ content increased to 0.86 apfu in sample Tpva) according to the redox reaction (1). The oxidation of Fe^{2+} and Mn^{2+}, traced by the Mössbauer and optical absorption data, is further supported by the decrease of the

FTIR-band intensities related to the O1 and O3 sites (see above) as well as by the bond-valence analysis (Table 8). For sample Tpva, BVS at the O3 (= V letter in the general formula) site (1.31 valence units, vu) clearly indicates that it is not fully occupied by (OH), but significant amounts of oxygen also occur at O3.

The bond-valence method may be useful to evaluate the presence of O^{2-} at O3. Of particular relevance in this regard is the plot of $^{O3}O^{2-}$ versus BVS at O3 of Bosi et al. (2018) showing an expected linear trend from BVS(O3) values of ~1.1 to ~2.0 vu. Note that the minimum BVS(O3) value of ~ 1.1 vu is consistent with the O3 site fully occupied by (OH), which forms a weak hydrogen bond with the closest O5 atom (O3–H···O5). The plot of data of samples Upva and Tpva in Bosi et al.'s (2018) diagram shows that they are consistent with data from other samples and the expected trend (Fig. 4). Note that in Bosi et al. (2018) was missing the data of sample BLSH2 from Ertl et al. (2012).

Conclusions

Single-crystal X-ray diffraction and spectroscopic data acquired after stepwise heating experiments at 700 °C of a natural Fe-rich princivalleite sample provide information on the induced structural and compositional response. Results show that the oxidation of Fe and Mn from + 2 to + 3 leads to variation in the color from pale blue to dark brown. A similar change in color to darker shades was also observed by Ertl et al. (2012) in a yellow Fe-free fluor-tsilaisite, ideally $NaMn_3Al_6(Si_6O_{18})(BO_3)_3(OH)_3F$, which, after heating in air at 750 °C for 30 h, changed color to dark brown–red due to the oxidation of Mn^{2+} to Mn^{3+}.

In our sample, the oxidation process is accompanied by significant deprotonation of the O1 and O3 sites, as confirmed by the progressive decrease in intensity of the bands above ~3600 cm^{-1} in the FTIR spectra during the heating experiments. However, the oxidation processes that Fe^{2+} and Mn^{2+} underwent are kinetically different, faster for Fe than Mn. In fact, almost all Fe^{2+} is oxidized after the treatment, whereas approximately one-third of the amount of Mn changed from + 2 to + 3. Structural data revealed that the ^{Y}Fe and ^{Y}Mn oxidation yield variations in the unit-cell parameters. Specifically, the decrease of the a-parameter is consistent with the oxidation of Fe^{2+} and Mn^{2+} and the consequent change in their ionic radius. On the other hand, the increase in the c-parameter during the treatment can be interpreted as a result of the increased content in ^{Z}(Fe, Mn).

This work represents the first in-depth investigation regarding the effects of heat treatment on a Fe-rich Mn-dominant tourmaline. In a previous study on a tourmaline sample with a slight enrichment in Mn (MnO ~ 1 wt%), a

similar thermal treatment (750 °C, 90 h) led to a complete oxidation of Mn from $+2$ to $+3$ (Bosi et al. 2021). Although the different oxidation rates observed for Mn and Fe can be the result of their distinctive redox standard potential, the incomplete oxidation of Mn^{2+} could be related either to the duration, the temperature, or to the initial content of Mn in the sample. For this reason, further investigations are required to characterize the different behavior of Mn and Fe during the oxidation process.

Declarations

Conflict of interest The authors declare that there is no conflict of interest.

References

Afonina GG, Bogdanova LA, Makagon VM (1993) Changes of Y and Z octahedra of tourmaline structure under its thermal working from X-ray powder patterns. ZVMO 122(6):89–98 (**in Russian**)

Altieri A, Pezzotta F, Skogby H, Hålenius U, Bosi F (2022) Blue growth zones caused by Fe^{2+} in tourmaline crystals from the San Piero in Campo gem-bearing pegmatites, Elba Island, Italy. Mineral Mag 86:910–919

Altieri A, Pezzotta F, Skogby H, Hålenius U, Bosi F (2023) Dark-coloured Mn-rich overgrowths in an elbaitic tourmaline crystal from the Rosina pegmatite, San Piero in Campo, Elba Island, Italy: witness of late-stage opening of the geochemical system. Mineral Mag 87:130–142

Andreozzi GB, Bosi F, Longo M (2008) Linking Mössbauer and structural parameters in elbaite-schorl-dravite tourmalines. Am Mineral 93:658–666

Bačík P, Ozdín D, Miglierini M, Kardošová P, Pentrák M, Haloda J (2011) Crystallochemical effects of heat treatment on Fe-dominant tourmalines from Dolní Bory (Czech Republic) and Vlachovo (Slovakia). Phys Chem Miner 8:599–611

Balan E, Radtke G, Fourdrin C, Paulatto L, Horn HA, Fuchs Y (2023) Effect of Fe-Fe interactions and X-site vacancy ordering on the OH-stretching spectrum of foitite. Eur J Mineral 35:105–116

Ballirano P, Celata B, Skogby H, Andreozzi GB, Bosi F (2022a) HT breakdown of Mn-bearing elbaite from the Anjanabonoina pegmatite, Madagascar. J Geosci 67:151–161

Ballirano P, Celata B, Bosi F (2022b) In-situ high-temperature behaviour and breakdown conditions of uvite at room pressure. Phys Chem Miner 49:40

Ballirano P, Celata B, Bosi F, Beckett-Brown CE, Andreozzi GB (2023) Thermal behavior of schorl up to breakdown temperature at room pressure. Period Mineral 92:23–32

Bosi F (2014) Bond valence at mixed occupancy sites. I. Regular polyhedra. Acta Crystallogr B70:864–870

Bosi F (2018) Tourmaline crystal chemistry. Am Mineral 103:298–306

Bosi F, Lucchesi S (2007) Crystal chemical relationships in the tourmaline group: structural constraints on chemical variability. Am Mineral 92:1054–1063

Bosi F, Skogby H, Hålenius U (2016a) Thermally induced cation redistribution in Fe-bearing oxy-dravite and potential geothermometric implications. Contrib Mineral Petrol 171:47

Bosi F, Skogby H, Balić-Žunić T (2016b) Thermal stability of extended clusters in dravite: a combined EMP, SREF and FTIR study. Phys Chem Mineral 43:395–407

Bosi F, Reznitskii L, Hålenius U, Skogby H (2017) Crystal chemistry of Al-V-Cr oxy-tourmalines from Sludyanka complex, Lake Baikal, Russia. Eur J Mineral 29:457–472

Bosi F, Skogby H, Hålenius U, Ciriotti M (2018) Experimental cation redistribution in the tourmaline lucchesiite, $CaFe^{2+}_3Al_6(Si_6O_{18})(BO_3)_3(OH)_3O$. Phys Chem Miner 45:621–632

Bosi F, Skogby H, Hålenius U (2019) Thermally induced cation redistribution in fluor-elbaite and Fe-bearing tourmalines. Phys Chem Mineral 46:371–383

Bosi F, Celata B, Skogby H, Hålenius U, Tempesta G, Ciriotti ME, Bittarello E, Marengo A (2021) Mn-bearing purplish-red tourmaline from the Anjanabonoina pegmatite, Madagascar. Mineral Mag 85:242–253

Bosi F, Pezzotta F, Skogby H, Altieri A, Hålenius U, Tempesta G, Cempirek J (2022) Princivalleite, $Na(Mn_2Al)Al_6(Si_6O_{18})(BO_3)_3(OH)_3O$, a new mineral species of the tourmaline supergroup from Veddasca Valley, Varese, Italy. Mineral Mag 86:78–86

Brown ID, Altermatt D (1985) Bond-valence parameters obtained from a systematic analysis of the inorganic crystal structure database. Acta Crystallogr B 41:244–247

Celata B, Ballirano P, Andreozzi G, Bosi F (2021) In-situ high-temperature behaviour of fluor-elbaite: breakdown conditions and products. Phys Chem Min 48:24

Dutrow BL, Henry DJ (2011) Tourmaline: a geologic DVD. Elements 7:301–306

Ertl A, Rossman GR, Hughes JM, Prowatke S, Ludwig T (2005) Mn-bearing "oxy-rossmanite" with tetrahedrally coordinated Al and B from Austria: Structure, chemistry and infrared and optical spectroscopic study. Am Min 90:481–487

Ertl A, Kolitsch U, Dyar MD, Hughes JM, Rossman GR, Pieczka A, Henry DJ, Pezzotta F, Prowatke S, Lengauer CL, Körner W, Brandstätter F, Francis CA, Prem M, Tillmanns E (2012) Limitations of Fe^{2+} and Mn^{2+} site occupancy in tourmaline: evidence from Fe^{2+}- and Mn^{2+}-rich tourmaline. Am Mineral 97:1402–1416

Filip J, Bosi F, Novák M, Skogby H, Tuček J, Čuda J, Wildner M (2012) Redox processes of iron in the tourmaline structure: example of the high-temperature treatment of Fe^{3+}-rich schorl. Geochim Cosmochim Acta 86:239–256

Fuchs Y, Fourdrin C, Balan E (2022) Theoretical OH stretching vibrations in dravite. Eur J Mineral 34:239–251

Grew ES, Krivovichev SV, Hazen RM, Hystad G (2016) Evolution of structural complexity in boron minerals. Can Mineral 54:125–143

Henry DJ, Dutrow BL (1992) Tourmaline in a low grade clastic metasedimentary rock: an example of the petrogenetic potential of tourmaline. Contrib Mineral Petrol 112:203–218

Henry DJ, Dutrow BL (1996) Metamorphic tourmaline and its petrologic applications. In: Grew ES, Anvitz LM (eds) Boron: mineralogy, petrology and geochemistry, reviews in mineralogy and geochemistry, vol 33. Mineralogical Society of America, Chantilly, Virginia, pp 503–557

Henry DJ, Novák M, Hawthorne FC, Ertl A, Dutrow B, Uher P, Pezzotta F (2011) Nomenclature of the tourmaline supergroup minerals. Am Mineral 96:895–913

Hovis GL, Tribaudino M, Altomare C, Bosi F (2023) Thermal expansion of minerals in the tourmaline supergroup. Am Mineral. https://doi.org/10.2138/am-2022-8580

Liu X, Yu C, Yang W, Xie L, Liang S (2019) Thermal decomposition kinetics of Fe-rich tourmaline. Eur J Mineral 31:919–928

Lussier AJ, Aguiar PM, Michaelis VK, Kroeker S, Herwig S, Abdu Y, Hawthorne FC (2008) Mushroom elbaite from the Kat Chay mine, Momeik, near Mogok, Myanmar: I. Crystal chemistry by SREF, EMPA, MAS NMR and Mössbauer spectroscopy. Mineral Mag 72:747–761

Lussier AJ, Hawthorne FC, Aguiar PM, Michaelis VK, Kroeker S (2011) Elbaite-liddicoatite from black rapids glacier, Alaska. Period Mineral 80:57–73

Mattson SM, Rossman GR (1984) Ferric iron in tourmaline. Phys Chem Mineral 11:225–234

Mattson SM, Rossman GR (1987) Fe^{2+}-Fe^{3+} interactions in tourmaline. Phys Chem Mineral 14:163–171

Novák M, Ertl A, Povondra P, Vašinová Galiová M, Rossman GR, Pristacz H, Prem M, Giester G, Gadas P, Škoda R (2013) Darrell-henryite, $Na(LiAl_2)Al_6(BO_3)_3Si_6O_{18}(OH)_3O$, a new mineral from the tourmaline supergroup. Am Min 98:1886–1892

Pesquera A, Gil-Crespo PP, Torres-Ruiz F, Torres-Ruiz J, Roda-Robles E (2016) A multiple regression method for estimating Li in tourmaline from electron microprobe analyses. Mineral Mag 80:1129–1133

Pieczka A, Kraczka J (2004) Oxidized tourmalines – a combined chemical, XRD and Mössbauer study. Eur J Mineral 16:309–321

Pouchou JL, Pichoir F (1991) Quantitative analysis of homogeneous or stratified microvolumes applying the model "PAP." In: Heinrich KFJ, Newbury DE (eds) Electron probe quantitation. Plenum, New York, pp 31–75

Prescher C, McCammon C, Dubrowinsky L (2012) MossA: a program for analyzing energy-domain Mössbauer spectra from conventional and synchrotron sources. J Appl Cryst 45:329–331

Reinitz I, Rossman GR (1988) Role of natural radiation in tourmaline coloration. Am Min 73:822–825

Sheldrick GM (2013) SHELXL2013. University of Göttingen, Germany

Slack JF, Trumbull RB (2011) Tourmaline as a recorder of ore-forming processes. Elements 7:321–326

Taran MN, Lebedev AS, Platonov AN (1993) Optical absorption spectroscopy of synthetic tourmalines. Phys Chem Mineral 20:209–220

van Hinsberg VJ, Schumacher JC (2011) Tourmaline as a petrogenetic indicator mineral in the Haut-Allier metamorphic suite, Massif Central, France. Can Mineral 29:177–194

van Hinsberg VJ, Henry DJ, Marschall HR (2011) Tourmaline: an ideal indicator of its host environment. Can Mineral 49:1–16

Watenphul A, Burgdorf M, Schlüter J, Horn I, Malcherek T, Mihailova B (2016) Exploring the potential of Raman spectroscopy for crystallochemical analyses of complex hydrous silicates: II. Tourmalines, Am Mineral 101:970–985

Wright SE, Foley JA, Hughes JM (2000) Optimization of site occupancies in minerals using quadratic programming. Am Mineral 85:524–531